Nonlinear analysis of free-electron-laser amplifiers in three dimensions

A. K. Ganguly and H. P. Freund*
Naval Research Laboratory, Washington, D.C. 20375
(Received 30 May 1985)

The nonlinear evolution of the free-electron-laser amplifier is investigated numerically for a configuration consisting of a helical wiggler and axial guide magnetic fields. A set of coupled nonlinear differential equations is derived in three dimensions which governs the self-consistent evolution of either the TE or TM modes in a loss-free cylindrical waveguide and the trajectories of an ensemble of electrons. The initial conditions are chosen to model the adiabatic injection of a cold, cylindrically symmetric electron beam into an interaction region in which the wiggler amplitude rises slowly from zero to a constant level in ten wiggler periods. Both self-field and space-charge effects have been neglected in the formulation, and the analysis is valid for the high-gain Compton regime of operation. Numerical simulations are conducted to model an amplifier operating in the neighborhood of 35 GHz, and for electron-beam energies of 250 keV and 1 MeV. (The free-electron-laser operating at electron-beam energies less than 500 keV is called the ubitron.) The growth rate in the linear regime prior to saturation is found to be in substantial agreement with the predictions based on a linear theory of the instability, and the saturation efficiency is consistent with that expected on the basis of simple, heuristic phase-trapping arguments. Substantial enhancements in the efficiency are found to occur due to the presence of the axial guide field.

I. INTRODUCTION

The free-electron laser (FEL) and the "ubitron" have been successfully demonstrated for operation over a broad frequency range from the microwave to the optical parts of the spectrum and show promise as a high-power source of radiation at millimeter and submillimeter wavelengths.[1–11] The distinction between the ubitron and the FEL is not well defined in the literature. In our work, we find it convenient to distinguish between the FEL and the ubitron primarily on the basis of the electron-beam energy, and we shall refer to such devices as ubitrons when the electron-beam energy is less than or of the order of 500 keV. While this choice of energy is arbitrary, it is motivated by the fact that most devices that operate at energies below 500 keV are characterized by operation frequencies that occur close to the waveguide cutoff. The ubitron[12] therefore, may be thought of as a weakly relativistic FEL operated as a microwave tube, and we emphasize that the physical mechanisms for the FEL and the ubitron are identical.

The motivation for the present work is to develop a fully three-dimensional nonlinear analysis of and simulation code for the FEL and the ubitron. Theoretical investigations of the ubitron and the FEL have been confined, principally, to the linear regime;[13–24] however, a fully nonlinear treatment is required to describe the interaction through the linear stages to saturation. We judged it important to include the effect of an axial guide magnetic field on the interaction in the analysis because (1) axial guide fields are included in many experimental configurations to confine high-current electron beams against the effects of self-fields, (2) linear analyses of the interaction have shown that substantial enhancements in the gain are possible due to the presence of the guide field, and (3) nonlinear simulation in one dimension has shown corresponding enhancements in the saturation efficiency. Three-dimensional effects become important when the transverse quiver velocity due to the wiggler magnetic field becomes large. In this regime, displacement of the electron from the axis of symmetry also becomes large, and a one-dimensional approximation for the wiggler magnetic field breaks down. In addition, the transverse-mode structure of the radiation field is important in the description of the overlap of the radiation field and the electron beam and is a crucial feature of the analysis when the interaction occurs in the vicinity of the waveguide cutoff in ubitrons.

In this paper we derive a fully three-dimensional nonlinear analysis of the FEL and the ubitron for a configuration in which an energetic electron beam is propagating through a loss-free cylindrical waveguide in the presence of a helically symmetric wiggler and a uniform axial guide field. To this end, a set of coupled nonlinear differential equations is derived which self-consistently describes the evolution of both an ensemble of electrons and the electromagnetic fields. Space-charge fields are neglected in the analysis; therefore, the treatment is applicable to the high-gain Compton (or strong-pump) regime. The nonlinear current which mediates the interaction is computed from the microscopic behavior of an ensemble of electrons by means of an average of the electron phases relative to the ponderomotive wave formed by the beating of the radiation and wiggler fields. These equations are solved for the case in which a monoenergetic electron beam of arbitrary initial cross section is adiabatically injected into the interaction region. The adiabatic injection is modeled by allowing the wiggler-field amplitude to increase slowly from zero in ten wiggler periods. The finite waveguide geometry is included in the analysis

by the introduction of the boundary conditions appropriate for either the transverse-electric (TE) or transverse-magnetic (TM) modes in a loss-free cylindrical waveguide. Thus, all transverse and finite-geometry effects are included in the static wiggler and radiation fields in a self-consistent manner. In addition, since the problem of interest is that of a ubitron and a FEL amplifier, only single-wave-mode propagation is considered. This permits an average over a wave period to be performed which eliminates the fast-time-scale phenomena from the formulation. The resulting equations are equivalent to a kinetic description of the problem and result in a great increase in computational efficiency over a full-scale particle-in-cell simulation.

The organization of the paper is as follows. The general equations are derived in Sec. II. The numerical solution of the coupled particle and field equations is given in Sec. III for parameters appropriate to both ubitrons and FEL's. A summary and discussion is given in Sec. IV.

II. GENERAL EQUATIONS

The physical configuration we employ includes a uniform axial guide field and a helically symmetric wiggler field generated by a bifilar helix, so that the static magnetic field can be written in the form

$$\mathbf{B}(\mathbf{x})=B_0\hat{\mathbf{e}}_z+\mathbf{B}_w(\mathbf{x}) , \tag{1}$$

where

$$\mathbf{B}_w(\mathbf{x})=2B_w(z)\left[I_1'(\lambda)\hat{\mathbf{e}}_r\cos\chi - \frac{1}{\lambda}I_1(\lambda)\hat{\mathbf{e}}_\theta\sin\chi+I_1(\lambda)\hat{\mathbf{e}}_z\sin\chi \right] \tag{2}$$

represents the wiggler field in cylindrical coordinates. In Eq. (2), $B_w(z)$ describes the wiggler amplitude, $\lambda\equiv k_w r$, $\chi\equiv\theta-k_w z$, $k_w(\equiv 2\pi/\lambda_w$, where λ_w is the wiggler period) is the wiggler wave number, and $I_n(\lambda)$ and $I_n'(\lambda)$ represent the modified Bessel function of order n and its derivative, respectively. The adiabatic injection of the electron beam is described by allowing the wiggler amplitude to vary slowly in z, which is a valid representation as long as

$$\frac{d}{dz}\ln B_w \ll k_w .$$

In practice, we shall allow $B_w(z)$ to vary only over $0\le z\le 10\lambda_w$, after which it shall be held constant. In the simulation it is assumed that

$$B_w(z)=\begin{cases} B_w\sin^2(k_w z/40), & 0\le z\le 10\lambda_w \\ B_w, & z>10\lambda_w . \end{cases} \tag{3}$$

Since the space-charge fields are neglected, the boundary conditions at the waveguide wall may be satisfied by expanding the vector potential in terms of the orthogonal basis functions of the empty guide. Thus, we write the vector potential of the radiation field in the form

$$\delta\mathbf{A}(\mathbf{x},t)=\sum_{\substack{l=0\\n=1}}^{\infty}\delta A_{ln}(z)\left[\frac{l}{k_{ln}r}J_l(k_{ln}r)\hat{\mathbf{e}}_r\sin\alpha_l + J_l'(k_{ln}r)\hat{\mathbf{e}}_\theta\cos\alpha_l \right] \tag{4}$$

for the TE modes, and

$$\delta\mathbf{A}(\mathbf{x},t)=\sum_{\substack{l=0\\n=1}}^{\infty}\delta A_{ln}(z)\left[J_l'(k_{ln}r)\hat{\mathbf{e}}_r\cos\alpha_l - \frac{l}{k_{ln}r}J_l(k_{ln}r)\hat{\mathbf{e}}_\theta\sin\alpha_l + \frac{k_{ln}}{k}J_l(k_{ln}r)\hat{\mathbf{e}}_z\sin\alpha_l \right] \tag{5}$$

for the TM modes, where for frequency ω and wave number $k(z)$

$$\alpha_l\equiv\int_0^z dz'k(z)+l\theta-\omega t . \tag{6}$$

In Eqs. (4)–(6), J_l and J_l' represent the regular Bessel function of the first kind of order l and its derivative, and k_{ln} describes the cutoff wave number. In the case of the TE_{ln} mode $k_{ln}\equiv x_{ln}'/R_g$, where $J_l'(x_{ln}')=0$ and R_g is the waveguide radius. For the TM_{ln} mode $k_{ln}\equiv x_{ln}/R_g$, where $J_l(x_{ln})=0$. Thus, there is an implicit limitation on the magnitude of the beam currents which can be treated self-consistently, and it is assumed that the mode amplitude $\delta A_{ln}(z)$ and wave number $k(z)$ are both slowly varying functions of z such that both

$$\frac{d}{dz}\ln[\delta A_{ln}(z)]\ll k ,$$

and

$$\frac{d}{dz}\ln[k(z)]\ll k .$$

The microscopic source current can be written as the following sum over identical particle trajectories:

$$\delta\mathbf{J}(x,t)=-en_b\frac{L}{N_T}\sum_{i=1}^{N_T}\mathbf{v}_i(z;x_{i0},y_{i0},t_{i0})\times\frac{\delta(t-\tau_i(z;x_{i0},y_{i0},t_{i0}))}{|v_{zi}(z;x_{i0},y_{i0},t_{i0})|} , \tag{7}$$

where L is the length of the interaction region, N_T is the total number of electrons, n_b is the average electron density, $\mathbf{v}_i(z;x_{i0},y_{i0},t_{i0})$ is the velocity of the ith electron at position z which entered the interaction region (i.e., crossed the $z=0$ plane) at time t_{i0} and transverse position (x_{i0},y_{i0}), and

$$\tau_i(z;x_{i0},y_{i0},t_{i0})=t_{i0}+\int_0^z\frac{dz'}{v_{zi}(z';x_{i0},y_{i0},t_{i0})} . \tag{8}$$

The system is assumed to be quasistatic in the sense that particles which enter the interaction region at times t_0 separated by integral multiples of a wave period will execute identical trajectories. As a result, $\mathbf{v}_i(z;x_{i0},y_{i0},t_{i0}+2\pi N/\omega)=\mathbf{v}_i(z;x_{i0},y_{i0},t_{i0})$ for integer N. The discrete sum over particles can be replaced by an integration over initial conditions, and we may rewrite (7) in the form

$$\delta\mathbf{J}(x,t)=-en_b v_{z0}\int_{A_g}\int dx_0dy_0\sigma_\perp(x_0,y_0)\int_{-T/2}^{T/2}dt_0\sigma_{||}(t_0)\mathbf{v}(z;x_0,y_0,t_0)\frac{\delta(t-\tau(z;x_0,y_0,t_0))}{|v_z(z;x_0,y_0,t_0)|}\ , \tag{9}$$

where v_{z0} is the initial axial velocity, $A_g\equiv\pi R_g^2$ is the cross-sectional area of the waveguide, $T\equiv L/v_{z0}$, and $\sigma_\perp(x_0,y_0)$ and $\sigma_{||}(t_0)$ describe the distribution of the initial conditions subject to the normalization

$$\int_{A_g}\int dx_0dy_0\sigma_\perp(x_0,y_0)=A_b\ , \tag{10}$$

$$\int_{-T/2}^{T/2}dt_0\sigma_{||}(t_0)=T\ , \tag{11}$$

where A_b is the cross-sectional area of the electron beam.

Substitution of the microscopic fields and the source current density into Maxwell's equations for the TE mode yields

$$\frac{d^2}{dz^2}\delta a_{ln}+\left[\frac{\omega^2}{c^2}-k^2-k_{ln}^2\right]\delta a_{ln}=\frac{\omega_b^2}{c^2}\beta_{z0}H_{ln}\left\langle\frac{v_1T_l^{(+)}+v_2W_l^{(+)}}{|v_z|}\right\rangle \tag{12}$$

and

$$2k^{1/2}\frac{d}{dz}(k^{1/2}\delta a_{ln})=\frac{\omega_b^2}{c^2}\beta_{z0}H_{ln}\left\langle\frac{v_1W_l^{(-)}-v_2T_l^{(-)}}{|v_z|}\right\rangle\ , \tag{13}$$

where

$$\delta a_{ln}\equiv e\delta A_{ln}/mc^2,\ \beta_{z0}\equiv v_{z0}/c,\ \omega_b^2\equiv 4\pi e^2n_b/m\ ,$$

and v_1, v_2 are the transverse components of the electron velocity relative to the basis vectors

$$\hat{e}_1=\hat{e}_x\cos(k_wz)+\hat{e}_y\sin(k_wz)$$

and

$$\hat{e}_2=-\hat{e}_x\sin(k_wz)+\hat{e}_y\cos(k_wz)\ .$$

For the TM mode, we find the similar result:

$$\frac{d^2}{dz^2}\delta a_{ln}+\left[1+\frac{k_{ln}^2}{k^2}\right]\left[\frac{\omega^2}{c^2}-k^2-k_{ln}^2\right]\delta a_{ln}=\frac{\omega_b^2}{c^2}\beta_{z0}H_{ln}\left\langle\frac{v_1T_l^{(+)}+v_2W_l^{(+)}+2\frac{k_{ln}}{k}v_zJ_l(k_{ln}r)\sin\alpha_l}{|v_z|}\right\rangle \tag{14}$$

and

$$2\left[k+\frac{k_{ln}^2}{k}\right]^{1/2}\frac{d}{dz}\left[\left[k+\frac{k_{ln}^2}{k}\right]^{1/2}\delta a_{ln}\right]=\frac{\omega_b^2}{c^2}\beta_{z0}H_{ln}\left\langle\frac{v_1W_l^{(-)}-v_2T_l^{(-)}+2\frac{k_{ln}}{k}v_zJ_l(k_{ln}r)\cos\alpha_l}{|v_z|}\right\rangle . \tag{15}$$

In the preceding equations, H_{ln}, $T_l^{(\pm)}$, and $W_l^{(\pm)}$ are mode- (i.e., polarization-) dependent quantities defined as

$$H_{ln}=\begin{cases}\dfrac{(x_{ln}'^2)}{[(x_{ln}'^2)-l^2]J_l^2(x_{ln}')}, & \text{TE}_{ln}\text{ mode}\\ \dfrac{1}{[J_l'(x_{ln})]^2}, & \text{TM}_{ln}\text{ mode}\end{cases} \tag{16}$$

and

$$T_l^{(\pm)}\equiv\begin{cases}F_l^{(\pm)}\sin\psi_l+G_l^{(\pm)}\cos\psi_l, & \text{TE}_{ln}\text{ mode}\\ F_l^{(\mp)}\cos\psi_l-G_l^{(\mp)}\sin\psi_l, & \text{TM}_{ln}\text{ mode}\end{cases} \tag{17}$$

$$W_l^{(\pm)}\equiv\begin{cases}F_l^{(\mp)}\cos\psi_l-G_l^{(\mp)}\sin\psi_l, & \text{TE}_{ln}\text{ mode}\\ -(F_l^{(\pm)}\sin\psi_l+G_l^{(\pm)}\cos\psi_l), & \text{TM}_{ln}\text{ mode}\end{cases} \tag{18}$$

where

$$\psi_l\equiv\psi_0+\int_0^z dz'\left[k+lk_w-\frac{\omega}{v_z}\right] \tag{19}$$

is the phase relative to the ponderomotive frame, $\psi_0(\equiv -\omega t_0)$ is the initial phase,

$$F_l^{(\pm)} \equiv J_{l-1}(k_{ln}r)\cos[(l-1)\chi] \pm J_{l+1}(k_{ln}r)\cos[(l+1)\chi] , \tag{20}$$

and

$$G_l^{(\pm)} \equiv J_{l-1}(k_{ln}r)\sin[(l-1)\chi] \pm J_{l+1}(k_{ln}r)\sin[(l+1)\chi] . \tag{21}$$

Finally,

$$\langle F \rangle \equiv \frac{1}{2\pi^2 R_g^{\,2}} \int_{-\pi}^{\pi} d\psi_0 \sigma_{\|}(\psi_0) \int_{A_g} \int d\theta_0 dr_0 r_0 \sigma_{\perp}(r_0,\theta_0) F \tag{22}$$

describes the average of the beam electrons over both the axial phase and cross section of the waveguide. It is important to recognize that this average includes the effect of the overlap of the electron beam with the transverse-mode structure of the radiation field (often included in one-dimensional formulations in an *ad hoc* manner by the inclusion of a filling factor) in a self-consistent way.

In order to complete the formulation, the electron-orbit equations in the presence of the static and fluctuation fields must be specified. Since we describe an amplifier configuration, we choose to integrate in z and write the Lorentz force equation in the form

$$v_z \frac{d}{dz}\mathbf{p} = -e\delta\mathbf{E}_{ln} - \frac{e}{c}\mathbf{v}\times(\mathbf{B}_0+\mathbf{B}_w+\delta\mathbf{B}_{ln}) , \tag{23}$$

where

$$\delta\mathbf{E}_{ln} = -\frac{1}{c}\frac{\partial}{\partial t}\delta\mathbf{A}_{ln}, \quad \delta\mathbf{B}_{ln} = \nabla\times\delta\mathbf{A}_{ln} .$$

Substitution of the appropriate form for the vector potential shows that

$$v_z \frac{d}{dz}p_1 = -\frac{1}{\gamma}[\Omega_0 - \gamma k_w v_z + 2\Omega_w I_1(\lambda)\sin\chi]p_2 + \frac{1}{\gamma}\Omega_w p_z I_2(\lambda)\sin(2\chi) - \tfrac{1}{2}mc\delta a_{ln}[(\omega - kv_z)W_l^{(-)} - 2k_{ln}v_2 J_l(k_{ln}r)\cos\alpha_l - \Gamma_{ln}v_z T_l^{(+)}] , \tag{24}$$

$$v_z \frac{d}{dz}p_2 = \frac{1}{\gamma}[\Omega_0 - \gamma k_w v_z + 2\Omega_w I_1(\lambda)\sin\chi]p_1 - \frac{1}{\gamma}\Omega_w p_z[I_0(\lambda)+I_2(\lambda)\cos(2\chi)] + \tfrac{1}{2}mc\delta a_{ln}[(\omega - kv_z)T_l^{(-)} - 2k_{ln}v_1 J_l(k_{ln}r)\cos\alpha_l + \Gamma_{ln}v_z W_l^{(+)}] , \tag{25}$$

$$v_z \frac{d}{dz}p_z = \frac{1}{\gamma}\Omega_w p_2[I_0(\lambda)+I_2(\lambda)\cos(2\chi)] - \frac{1}{\gamma}\Omega_w p_1 I_2(\lambda)\sin(2\chi) - \tfrac{1}{2}mc\delta a_{ln}[k(v_1 W_l^{(-)} - v_2 T_l^{(-)}) + \Gamma_{ln}(v_1 T_l^{(+)} + v_2 W_l^{(+)})] , \tag{26}$$

for the TE_{ln} mode, where $\Omega_{0,w} \equiv |eB_{0,w}/mc|$, $\gamma \equiv (1-v^2/c^2)^{-1/2}$ is the relativistic factor, $\mathbf{p}$ is the momentum, and

$$\Gamma_{ln} \equiv \frac{d}{dz}(\ln\delta a_{ln})$$

represents the growth rate of the wave mode. For the TM_{ln} mode, we find

$$v_z \frac{d}{dz}p_1 = -\frac{1}{\gamma}[\Omega_0 - \gamma k_w v_z + 2\Omega_w I_1(\lambda)\sin\chi]p_2 + \frac{1}{\gamma}\Omega_w p_z I_2(\lambda)\sin(2\chi) - \tfrac{1}{2}mc\delta a_{ln}\left[\left[\omega - \frac{k^2+k_{ln}^2}{k}v_z\right]W_l^{(-)} - \Gamma_{ln}v_z T_l^{(+)}\right] , \tag{27}$$

$$v_z \frac{d}{dz}p_2 = \frac{1}{\gamma}[\Omega_0 - \gamma k_w v_z + 2\Omega_w I_1(\lambda)\sin\chi]p_1 - \frac{1}{\gamma}\Omega_w p_z[I_0(\lambda)+I_2(\lambda)\cos(2\chi)] + \tfrac{1}{2}mc\delta a_{ln}\left[\left[\omega - \frac{k^2+k_{ln}^2}{k}v_z\right]T_l^{(-)} + \Gamma_{ln}v_z W_l^{(+)}\right] , \tag{28}$$

$$v_z \frac{d}{dz}p_z = \frac{1}{\gamma}\Omega_w p_2[I_0(\lambda)+I_2(\lambda)\cos(2\chi)] - \frac{1}{\gamma}\Omega_w p_1 I_2(\lambda)\sin(2\chi) - \tfrac{1}{2}mc\delta a_{ln}\left[\frac{k^2+k_{ln}^2}{k}(v_1 W_l^{(-)} - v_2 T_l^{(-)}) + \Gamma_{ln}(v_1 T_l^{(+)} + v_2 W_l^{(-)}) + 2\omega\frac{k_{ln}}{k}J_l(k_{ln}r)\cos\alpha_l\right] . \tag{29}$$

In addition, we have that for either the TE_{ln} or TM_{ln} modes

$$v_z \frac{d}{dz} x = v_1 \cos(k_w z) - v_2 \sin(k_w z) , \tag{30}$$

$$v_z \frac{d}{dz} y = v_1 \sin(k_w z) + v_2 \cos(k_w z) , \tag{31}$$

and

$$\frac{d}{dz} \psi_l = k + l k_w - \frac{\omega}{v_z} . \tag{32}$$

Both the linear and nonlinear evolution of the FEL and the ubitron amplifier are included in the formulation through Eqs. (12)—(15) for the fields, and (23)—(32) for the particles.

III. NUMERICAL SIMULATION

The set of coupled differential equations derived in Sec. II is solved numerically for an amplifier configuration in which a single wave of frequency ω is injected into the system at $z=0$. Maxwell's Eqs. (12)—(15) can be reduced to a set of three first-order differential equations for δa_{ln}, Γ_{ln}, and k. Hence, the numerical resolution of the problem consists in the simultaneous solution of $6N_T+3$ first-order ordinary differential equations, where N_T is the total number of electrons. The algorithm we employ involves the use of a fourth-order Runge-Kutta method to calculate the first three steps after the initial state, after which an Adams-Moulton predictor and corrector is employed for all further steps. The averages in Eqs. (12)—(15) are performed by means of an Nth-order Gaussian quadrature technique in each of the variables (ψ_0, r_0, θ_0); hence, $N^3 = N_T$. For all cases discussed in this work a choice of $N=10$ was found to provide an accuracy of better than 0.1%.

The initial state was chosen to model the injection of a solid, axisymmetric, monoenergetic electron beam of zero emittance and uniform cross section. Hence, we choose $\sigma_\perp = \sigma_\parallel = 1$, and initially set $\mathbf{p}_\perp = 0$ and $p_\parallel = mc(\gamma_0^2 - 1)^{1/2}$. In addition, the electron positions are chosen by means of the Gaussian algorithm within the ranges $-\pi \le \psi_0 \le \pi$, $0 \le \theta_0 < 2\pi$ and $R_{\min} \le r_0 \le R_{\max}$; hence, we may model the case of either a solid or an annular electron beam. Within the context of this beam geometry, the plasma frequency is related to the total beam current I_b by means of the relation

$$\omega_b^2 = \frac{4e}{m v_{z0}} \frac{I_b}{(R_{\max}^2 - R_{\min}^2)} . \tag{33}$$

In order to satisfy self-consistently the neglect of space-charge fields and treat the high-gain Compton regime, we must require that

$$\frac{\omega_b}{\gamma_0^{1/2} c k_w} \ll \frac{v_\perp^2}{c^2} \gamma_\parallel^3 \tag{34}$$

within the uniform-wiggler region. This limitation on the beam current will vary with the choice of energy, wiggler, and axial magnetic field strengths, and wiggler period, but will be adhered to in all the cases we study. The initial conditions on the radiation field are chosen such that $\Gamma_{ln}(z=0)=0$ and $k(z=0)=(\omega^2/c^2 - k_{ln}^2)^{1/2}$ for an arbitrary initial power level. Observe that the time-averaged Poynting flux P_ω for the waveguide mode is related to the field amplitude by the relation

$$P_\omega = \frac{m^2 c^4}{8e^2} \frac{R_g^2}{H_{ln}} \omega k \delta a_{ln}^2 \tag{35}$$

for the TE_{ln} mode, and

$$P_\omega = \frac{m^2 c^4}{8e^2} \frac{R_g^2}{H_{ln}} \omega \left[k + \frac{k_{ln}^2}{k} \right] \delta a_{ln}^2 . \tag{36}$$

for the TM_{ln} mode.

It is important to observe that, although the analysis applies to the high-gain Compton regime, collective effects are included through the dielectric response of the plasma to the waveguide mode, and the analysis is not purely for a single particle. Thus, while the wave number is set initially by means of the vacuum dispersion relation, the system evolves through an initial transient regime into a fully self-consistent dielectrically-loaded waveguide mode.

The first case we consider is that of a wide-band 35-GHz-ubitron amplifier operating in the TE_{11} mode. To this end, we assume a wiggler field with an amplitude and period of $B_w = 2$ kG and $\lambda = 1.175$ cm, and a waveguide radius of $R_g = 0.366\,26$ cm. The electron beam configuration is that of a solid (i.e., pencil) beam with an energy of 250 keV, a current of 35 A, and an initial radius of $R_{\max} = 0.155$ cm. The initial distributions in the axial phase space and the beam cross section are shown in Figs. 1 and 2. Each dot in the illustration of the axial phase space (Fig. 1) describes a "phase sheet" composed of 100 electrons, distributed throughout the cross section of the beam. Each phase sheet, therefore, represents a cross-sectional slice of the beam, which is chosen initially as shown in Fig. 2. The circle shown in Fig. 2 represents the waveguide wall. Each phase sheet is initially chosen to be identical; however, the subsequent evolution of the parti-

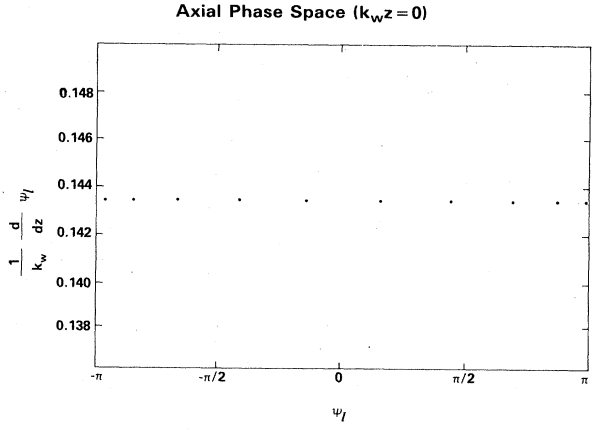

FIG. 1. Initialization of the axial phase space. Each point represents the superposition of 100 particles distributed throughout the cross section of the beam.

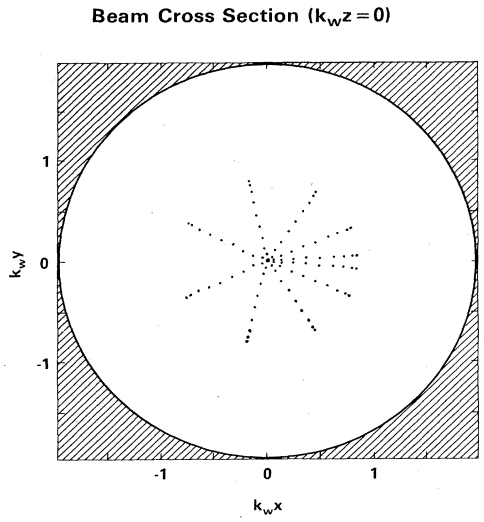

FIG. 2. Initialization of the beam cross section.

cle trajectories in the presence of the radiation field is followed self-consistently. It should be remarked that the particle distribution described herein represents a uniform electron beam. The positions (r_0,θ_0,ψ_{I0}) were chosen by a ten-point Gaussian weighting, and the nonuniformity in the positions of the electrons is compensated for by a nonuniform weighting of the particles.

We now digress, briefly, to describe the types of single-particle trajectory in the combined wiggler and axial guide magnetic fields. The optimum orbit for the FEL and ubitron operation is characterized by a coherent electron motion in phase with the wiggler. Such orbits would have a constant axial velocity (to preserve the resonance condition between the particles and the ponderomotive wave formed by the beating of the wiggler and radiation fields) as well as a transverse velocity of constant magnitude. A class of orbits of this type may be found in the presence of both a wiggler and an axial guide field.[25–27] These ideal orbits describe helical trajectories about the axis of symmetry (axicentered), and are characterized by

$$\mathbf{v}=v_w\hat{\boldsymbol{e}}_1+v_{||}\hat{\boldsymbol{e}}_z\ , \tag{37}$$

$\lambda=\mp v_w/v_{||}$, and $\chi=\pm\pi/2$, where $v_w,v_{||}$ are constants, and

$$v_w=\frac{2\Omega_w v_{||}I_1(\lambda)/\lambda}{\Omega_0-\gamma k_w v_{||}\pm 2\Omega_w I_1(\lambda)}\ . \tag{38}$$

The self-consistent solution for the axial velocity as a function of B_0, B_w, λ_w, and γ may be found by substitution of the expressions for γ and v_w into

$$v_{||}^2+v_w^2=(1-\gamma^{-2})c^2\ . \tag{39}$$

The solution is obtained by numerical means, and is shown in Fig. 3 as a function of B_0 for $B_w=2$ kG, $\lambda_w=1.175$ cm, and $V_b=250$ keV ($\gamma\simeq 1.489$). As shown in the figure, there are two types of orbit. Group-I orbits

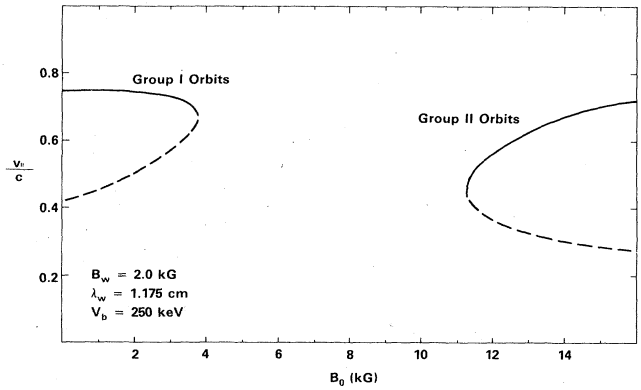

FIG. 3. Graph of the axial velocity as a function of the guide magnetic field for the ideal helical orbits.

are found for relatively low axial guide fields and are characterized by $\Omega_0<\gamma k_w v_{||}$. In contrast, group-II orbits occur for high axial fields and have $\Omega_0>\gamma k_w v_{||}$. The dashed line represents orbitally unstable trajectories.

The purpose of the adiabatic entry taper in the wiggler field is to inject electrons into the wiggler region onto trajectories approximating these ideal helical orbits. Numerical integration of the particle trajectories (i.e., in the absence of a radiation field) shows that such injection is feasible for particles initially on axis [i.e., $r(z=0)=0$] as long as the orbit parameters are not *too close* to the magnetic resonance at $\Omega_0\approx\gamma k_w v_{||}$. Thus, there are practical limitations on the operation of the ubitron and the FEL near magnetic resonance. Of course, the injection process is not perfect, and the orbits differ slightly from the ideal trajectories in that periodic motion is also observed corresponding to Larmor oscillations due to the axial guide field, betatron oscillations due to the transverse gradient in the wiggler field, and higher harmonics of the wiggler period. These problems intensify somewhat for electrons which are injected off axis [i.e., $r(z=0)>0$], in addition to which the magnitudes of the transverse and axial velocities of the ideal helical component of the motion vary with radial position. This occurs because the electrons "see" a higher average wiggler field as the displacement from the axis grows, and an electron injected at an initial radius of r_0 will be characterized by a wiggler velocity of[28]

$$v_w=\frac{2\Omega_w v_{||}I_0(\lambda_0)I_1(\lambda)/\lambda}{\Omega_0-\gamma k_w v_{||}\pm 2\Omega_w I_0(\lambda_0)I_1(\lambda)}\ , \tag{40}$$

where $\lambda_0\equiv k_w r_0$. As a consequence, the finite extension of the electron beam will correspond to a spread in $(v_w,v_{||})$ across the beam which, in turn, will result in a broadening of the wave-particle resonance. The net result of all of these effects is that the beam may display a very complex overall bulk motion, and we emphasize that all of these effects are included in the simulation in a self-consistent way.

In order to illustrate the particle trajectories which occur in the combined field structure, it is useful to show the evolution of the beam cross section at a series of axial

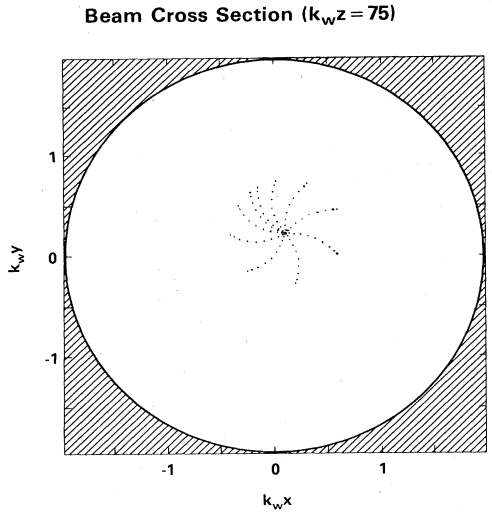

FIG. 4. Representation of the beam cross section at $k_w z = 75$, which is shortly after the start of the uniform wiggler region.

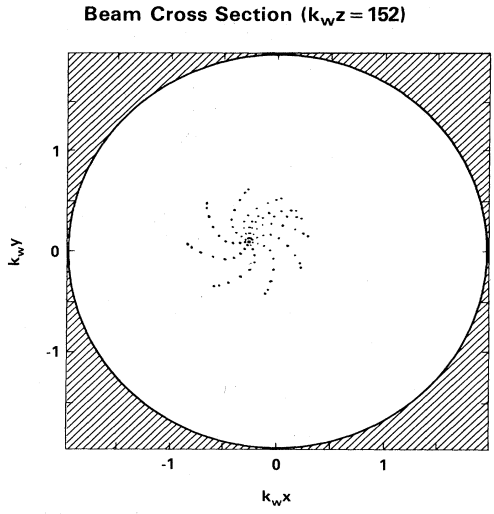

FIG. 6. Representation of the beam cross section at $k_w z = 152$.

positions within the interaction region. We consider a set of parameters consistent with group-I orbits and choose an axial field of $B_0 = 1.3$ kG. This is sufficiently far from the magnetic resonance (see Fig. 3) that injection onto near-ideal orbits is possible. In Fig. 4, we show the beam cross section at $k_w z = 75$, which corresponds to a point just after the start of the uniform wiggler region at $k_w z \simeq 62.83$. Note that the initial value of the radiation field was chosen to correspond to an input power of $P_{\text{in}} = 10$ W at a frequency $\omega / c k_w = 1.3$, so that the perturbation to the single-particle orbits at this point due to the electromagnetic field is negligible. It is immediately evident from the figure that the beam has been substantially compressed due to the focusing effect of the wiggler. In addition the beam center is shifted off axis corresponding to the helical motion imposed by the wiggler. Thus, the beam has "spun up" due to the transverse velocity v_w arising from the combined influence of the wiggler and guide magnetic fields. The injection process for these parameters yields orbits close to the ideal helical trajectories, and $k_w r_{\text{center}} \sim 0.25$ for the beam center which is in good agreement with the result expected from the ideal trajectories. The beam also displays a rotational motion about the center which is accounted for by the combined effects of the variation in v_w across the beam cross section and the betatron oscillation due to the transverse wiggler gradient.

The overall bulk motion of the beam is expected to display a periodicity at the fundamental wiggler harmonic and to twist the beam into a helix about the axis of symmetry. Such motion is observed as is shown in Figs. 5–8, which displays the beam cross section as it evolves from

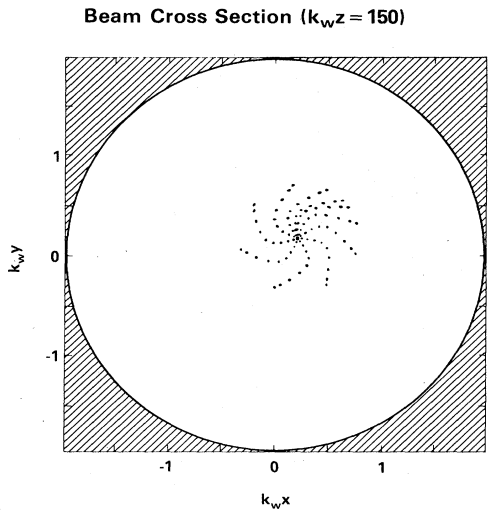

FIG. 5. Representation of the beam cross section at $k_w z = 150$, corresponding to the linear phase of the interaction.

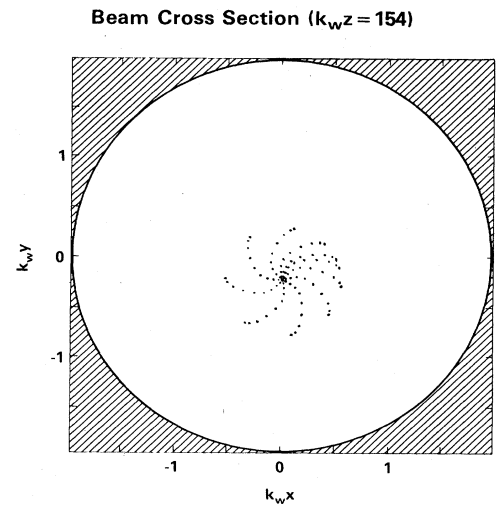

FIG. 7. Representation of the beam cross section at $k_w z = 154$.

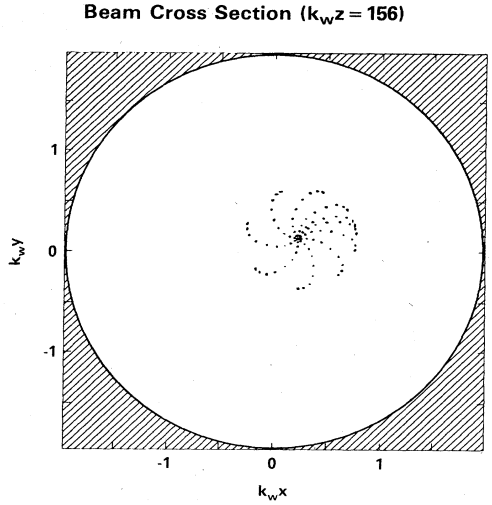

FIG. 8. Representation of the beam cross section at $k_w z = 156$.

$k_w z = 150$ through 156 (approximately one wiggler period). Note that this is well within the region of strong linear (i.e., exponential) growth of the radiation field, and substantial amplification of the input signal has occurred. As a result, each phase sheet has reacted in a slightly different way. This is indicated by the "smearing" of the dots in Figs. 5–8 which marks small displacements of the beam centers in each phase sheet as well as small differences in the rates of rotation about the beam centers. We conclude, therefore, that the motion of the beam includes an overall bulk helical motion about the symmetry axis at the wiggler period, as well as a "pinwheeling" type of rotation about the beam center at a much longer period.

The evolution of the waveguide mode corresponding to these transverse beam motions is shown in Fig. 9. The electromagnetic wave was a TE_{11} waveguide mode (for $R_g = 0.36626$ cm) at $\omega/ck_w = 1.3$ which corresponds to a frequency of $f = 33.2$ GHz. Beam voltage and current were 250 keV and 35 A, respectively, for an average beam power of 8.75 MW. As shown in the figure, the growth of the wave mode was approximately exponential after an initial transient period for $k_w z \lesssim 80$. During the linear phase of the interaction the growth rate was $\Gamma_{11}/k_w \simeq 0.029$, and a small increase was observed prior to saturation at $k_w z = 267$. The radiation power at saturation was 1.87 MW for an overall efficiency of $\eta = 21.4\%$. A complete spectrum of the efficiency at saturation versus frequency is shown in Fig. 10, in which the dots represent the numerical results of the simulation. We observe that peak efficiency occurs for $\omega_{\text{peak}} \sim 1.3ck_w$, with a bandwidth $\Delta\omega/\omega_{\text{peak}} \sim 54\%$.

Saturation is by means of particle trapping in the ponderomotive wave formed by the beating of the radiation and wiggler fields. This is clearly shown in Fig. 11 in which we plot the axial phase space at saturation for the case of $\omega/ck_w = 1.3$. The solid lines in the figure represent *approximate* separatrices calculated under the assumption that all particles are executing the ideal helical trajectories. Thus, the actual number of electrons trapped may differ slightly from that shown in the figure, but the conclusion remains valid. The beam cross section at saturation is shown in Fig. 12. Although the figure seems to show a chaotic state in which the initial uniformity in cross section of each phase sheet has been destroyed, a closer examination of the positions of the electrons within each phase sheet shows that the electron positions have retained their coherence and appear much as shown in Figs. 5–8. However, the beam centers in each phase sheet have shifted markedly so that the superposition of the electrons in all the phase sheets gives the appearance of a random distribution.

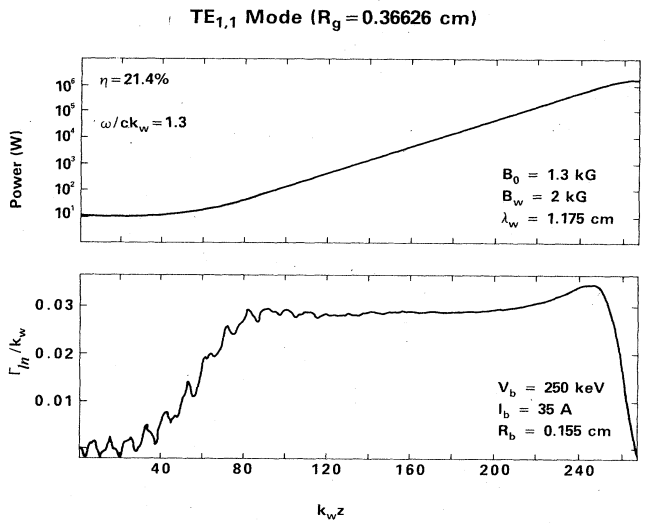

FIG. 9. Evolution of the radiation power and growth rate of the TE_{11} mode as a function of axial position.

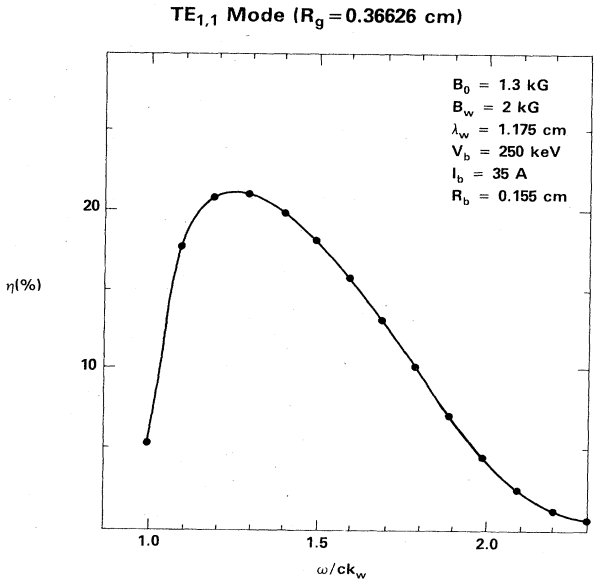

FIG. 10. Spectrum of the interaction efficiency vs frequency for the TE_{11} mode.

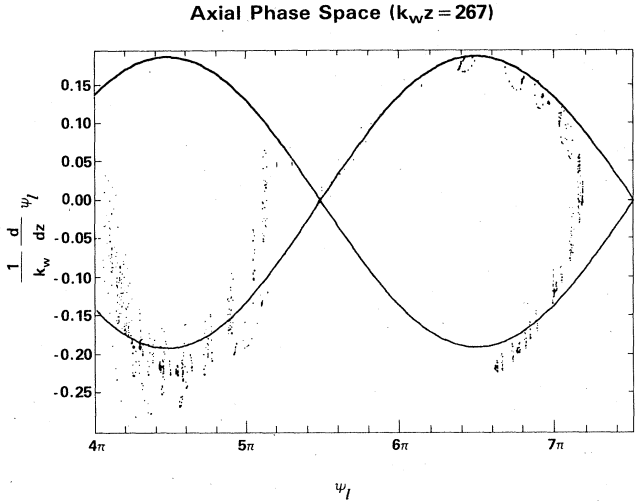

FIG. 11. Representation of the axial phase space at saturation.

The consistency of the code has been checked several ways. The most fundamental is the requirement of energy conservation between the particles and the wave, and agreement between the energy lost by the beam and that gained by the wave was found to be significantly better than 0.1% in all cases considered. In addition, the growth rate in the linear regime has been checked against the predictions of a three-dimensional linear theory of the interaction.[24] Although the linear theory represents an idealized model in which all particle trajectories are described by the ideal helical orbits, agreement between the simulation and the linear theory is good. At the frequency corresponding to peak efficiency ($\omega/ck_w = 1.3$), the linear theory predicts a growth rate of $\Gamma_{\rm lin}/k_w \simeq 0.031$, which compares well with the simulation result of $\Gamma_{11}/k_w \simeq 0.029$. Finally, an estimate of the efficiency on the basis of the simple heuristic phase-trapping model yields an estimate of a 19.1% efficiency, which is close to the 21.4% efficiency obtained from the simulation.

The case of the TM_{11} mode has also been examined using the simulation code. In order to facilitate comparison with the TE_{11} mode, the parameters specifying the external magnetic fields and electron beam remain unchanged; that is $B_0 = 1.3$ kG, $B_w = 2.0$ kG, $\lambda_w = 1.175$ cm, $V_b = 250$ keV, $I_b = 35$ A, and the initial beam radius is $R_b = 0.155$ cm. The only alteration is in the choice of the waveguide radius in order to shift the waveguide dispersion curve relative to the beam resonance line [i.e., $\omega = (k + k_w)v_{||}$]. We choose $R_g = 0.762\,23$ cm so that the waveguide cutoff is identical to that of the TE_{11} mode, and the interaction occurs over the same frequency band. Numerical results then yield a peak efficiency $\eta_{\rm max} \simeq 5.92\%$ at a frequency of $\omega/ck_w \simeq 1.78$. This is significantly lower than the peak efficiency of 21.4% found for the TE_{11} mode at a frequency of $\omega/ck_w \simeq 1.3$. The growth rate was also significantly lower, and we observe a growth rate of only $\Gamma_{11}/k_w \simeq 0.012$ at the frequency corresponding to peak efficiency. For this reason, we shall confine our attention in the remainder of this work to the TE modes. However, we emphasize that no attempt was made to optimize the interaction with respect to the TM_{11} mode, and it would be unjustified to conclude (as in the case of the gyrotron, for example) that the FEL and the ubitron interaction favors the TE mode.

The cases discussed thus far dealt with waveguide modes with an $l = 1$ azimuthal mode number. Examination of the dynamical equations shows that as long as χ is an approximate constant along the particle trajectories ($\chi = \pm\pi/2$ for the ideal helical orbits) a *selection rule* exists whereby TE_{ln} or TM_{ln} modes interact via wave-particle resonances at $\omega \simeq (k + lk_w)v_{||}$. It has been conjectured, therefore, that no interaction is possible for the $l = 0$ modes, and numerical study of test cases for TE_{01} and TM_{01} modes has, indeed, shown that no gain occurs.

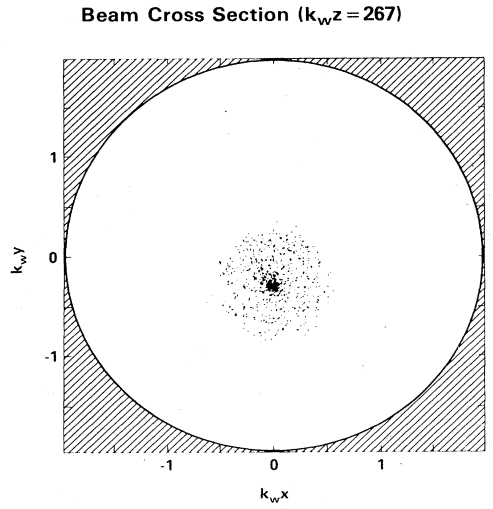

FIG. 12. Representation of the beam cross section at saturation.

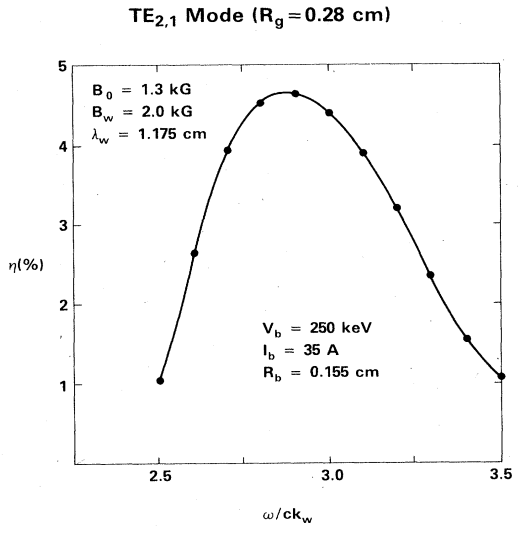

FIG. 13. Spectrum of the interaction efficiency vs frequency for the TE_{21} mode.

Higher harmonic interactions may also be studied by the selection of higher-order (i.e., $l>1$) modes, and the results of a series of simulations are shown in Fig. 13 for the TE_{21} mode. As in the case of the TM_{11} mode, the parameters specifying the external magnetic fields and the electron beam are chosen to be identical to those used to study the TE_{11} mode in order to facilitate comparison of the interaction at the two harmonics. Only the waveguide radius has been changed to $R_g=0.28$ cm in order to bring the intersection points between the TE_{21} dispersion curve and the beam resonance line, $\omega=(k+2k_w)v_{||}$, sufficiently close together to obtain a relatively broad-band gain spectrum. The growth rate found at the frequency which corresponds to peak efficiency (i.e., $\omega_{\text{peak}}/ck_w\simeq 2.9$) was $\Gamma_{21}/k_w\simeq 0.025$ which is comparable to that found for the TE_{11} mode ($\Gamma_{11}/k_w\simeq 0.029$ at $\omega/ck_w\simeq 1.3$). The efficiency is plotted as a function of frequency for the TE_{21} mode in Fig. 13. While the bandwidth $\Delta\omega/\omega_{\text{peak}}\simeq 43\%$ is comparable and the frequency is more than doubled relative to the TE_{11} mode, the peak efficiency of 4.7% is greatly decreased.

We now turn to the case of a higher-energy electron beam. In Fig. 14 we plot the variation of the axial velocity of the ideal helical orbits versus B_0 for 1-MeV electrons and a wiggler characterized by $B_w=1.0$ kG and $\lambda_w=3$ cm. As indicated in the figure, group-I orbits are found for axial guide fields $B_0\lesssim 6.4$ kG, and group-II orbits for $B_0\gtrsim 8.2$ kG. No such orbits are possible between these limiting values. The first case we consider is that of $B_0=3.5$ which corresponds to a group-I type of trajectory, and we assume a 1-MeV, 50-A electron beam with an initial radius of 0.2 cm. The waveguide radius was chosen to be $R_g=0.45$ cm, so the upper and lower intersection frequencies between the TE_{11} dispersion curve and the beam resonance line are well separated and occur at $\omega/ck_w=10.9$ and 2.8, respectively. Gain is, indeed, found in the vicinity of these frequencies, as shown in Fig. 15 in which we plot the interaction efficiency versus frequency for this case. We observe that the efficiency drops rapidly near the upper (lower) range of the lower (upper) frequency band. The lower frequency band corresponds to frequencies $f\sim 28$ GHz which are comparable to those found for the TE_{11} mode for a 250-keV beam, and although the bandwidth is narrower than that found previously (see Fig. 10) the efficiencies are comparable. The upper frequency range shows a broader bandwidth and somewhat reduces efficiency ($\eta_{\text{peak}}\sim 13.7\%$).

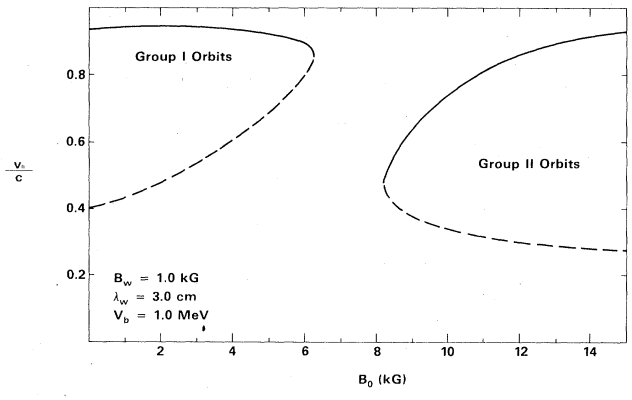

FIG. 14. Graph of the axial velocity as a function of the axial guide magnetic field for the ideal helical orbits.

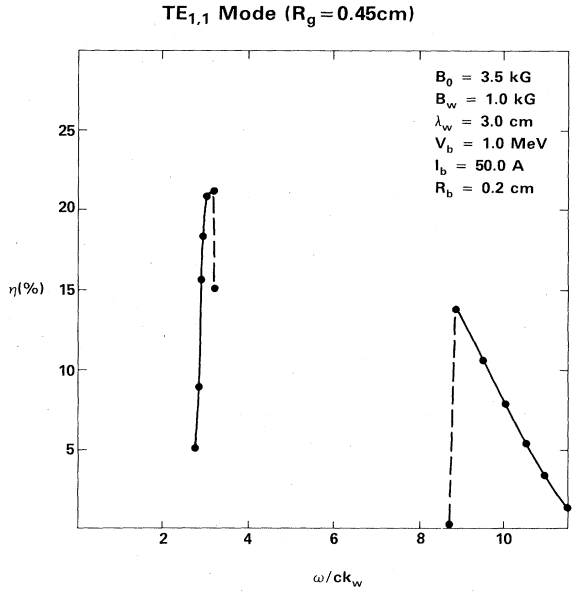

FIG. 15. Spectrum of the interaction efficiency vs frequency for the TE_{11} mode and parameters corresponding to group-I orbits.

The results of a series of simulations for $B_0=11.75$ kG and $R_g=0.5$ cm are shown in Fig. 16 for parameters con-

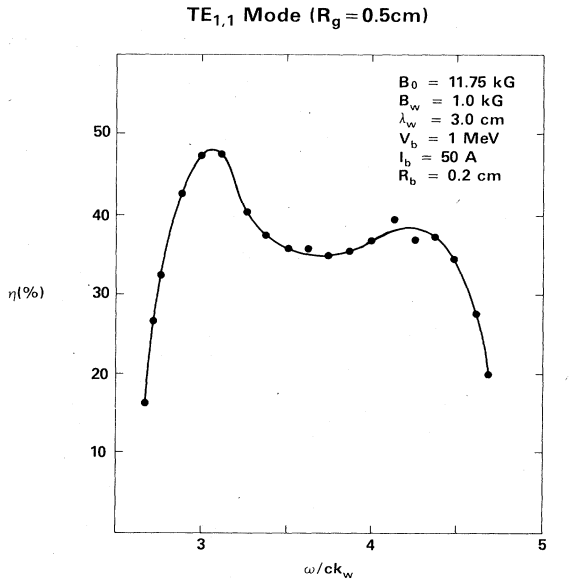

FIG. 16. Spectrum of the interaction efficiency vs frequency for the TE_{11} mode and parameters corresponding to group-II orbits.

sistent with group-II orbits, in which we plot the interaction efficiency as a function of frequency. It should be remarked that for some of these runs a *small fraction* of the beam was lost to the wall. The procedure followed when this occurred was to eject such particles from the simulation, and the efficiencies shown include this effect. The bandwidth observed was $\Delta\omega/\omega_{\text{peak}} \simeq 57\%$ over a frequency range of 28—45 GHz. However, while the frequency range is comparable to that used for the lower-energy (250-keV) case, the observed efficiencies are considerably higher. We observe a peak efficiency $\eta_{\text{peak}} \simeq 47\%$ at frequencies in the range $\omega_{\text{peak}}/ck_w \simeq 3.0$—$3.1$, which is more than double that found for the group-I orbits with a 1-MeV beam in this frequency range. It should be emphasized here that this efficiency is found with uniform wiggler and guide magnetic fields, and no magnetic field tapering was used. This enhancement in the interaction efficiency associated with group-II orbit parameters has also been observed in one-dimensional simulation.[29]

The small degree of variation in the efficiency about the line of best fit is difficult to account for precisely due to the complexity of the system of coupled equations. Some of the causes of this additional structure undoubtedly include the following: (1) variations in the number of particles which are lost to the wall, and the positions (in z) at which they are lost, (2) the variation in the ponderomotive potential with the frequency at which the interaction occurs, and (3) variations in the evolution of the radial profile of the beam near saturation (where the radiation field is large) which have an effect upon both the overall filling factor and the trapping fraction. However, this is an area of ongoing investigation, and we cannot rule out the possibility of an additional modulation of the interaction due to departures of the electron trajectories from the ideal helical orbits.

IV. SUMMARY AND CONCLUSIONS

In this paper we have developed a fully self-consistent nonlinear theory and numerical simulation of the ubitron and the FEL amplifier in three dimensions. The particular configuration considered consists of a cylindrically symmetric electron beam of arbitrary cross section injected into a loss-free cylindrical waveguide in the presence of both a helically symmetric wiggler and a uniform axial guide magnetic field. In addition, the adiabatic injection of the electron beam has been modeled by including an initial taper of the wiggler-field amplitude. The system of equations derived describes the self-consistent evolution of both the wave fields and the trajectories of an ensemble of electrons. The analysis has been performed for both the TE and TM modes, and describes the overlap of the transverse mode structure and the electron beam (i.e., the filling factor) in a self-consistent manner. Space-charge fields have been neglected in the analysis, so the treatment is applicable to the high-gain Compton regime of operation. In addition, self-field effects of the electron beam have been neglected. Since the problem of interest is in the ubitron and the FEL amplifier, only single-wave-mode propagation is considered. This permits an average over the wave period to be performed which eliminates the fast-time-scale phenomena from the formulation, and results in a great increase in computational efficiency over a full-scale particle-in-cell simulation code.

The electron trajectories are integrated using the exact Lorentz force equations, so that we are able to examine the detailed motion of the electron beam in the combined field structure. Overall bulk motion of the beam exhibits a dominant oscillation at the fundamental wiggler period, as expected, which twists the beam into a helix about the axis of symmetry. In addition, a significant focusing effect is observed to occur due to the radial inhomogeneity of the wiggler which can result in a significant contraction in the beam radius. Superimposed on this bulk motion is (1) a shear in the electron velocity across the beam, and (2) a slow-time-scale betatron oscillation whose net effect results in a slow pinwheeling motion about the beam center. Larmor motion due to the axial guide field is more difficult to identify because the period may be comparable (especially near magnetic resonance) to the wiggler period. However, the adiabatic beam-injection technique was found to be effective as long as the parameters were not too close to magnetic resonance, and the Larmor motion can be kept small.

Numerical simulations were conducted for parameters corresponding to a 250-keV ubitron and a 1-MeV FEL. In all cases, comparison of the energy lost by the particles to that gained by the wave showed energy to be conserved to within an accuracy significantly better than 0.1%. The consistency of the simulation was also checked by comparison of (1) the growth rate found by the code with that predicted from a linear theory of the instability,[24] and (2) the saturation efficiency obtained in the simulation with that found by simple phase-trapping arguments. In both cases, good agreement was found.

The parameters chosen to model the 250-keV ubitron and the 1-MeV FEL were chosen so that the output frequency was in the neighborhood of 35 GHz for both cases. In each case, the peak efficiency for the TE_{11} mode was found to be in the neighborhood of 20% for parameters corresponding to group-I trajectories (i.e., a relatively low axial guide field). However, the group-II type of trajectory was found to result in substantial enhancements in both the efficiency ($\sim 45\%$) and bandwidth for the case of the higher-energy (1-MeV) beam. This is consistent with the results found for a previous one-dimensional simulation of a 1.25-MeV beam. The amplification of the TM_{11} was also studied for parameters associated with the 250-keV ubitron, and found to result in substantially lower growth rates and saturation efficiencies than the TE_{11} mode. However, since no optimization of the parameters for the TM mode was attempted, it is premature to conclude that the FEL and the ubitron interaction favors the TE mode.

Higher harmonic interactions have also been studied, and arise from the azimuthal variation of the modes in a cylindrical waveguide. Since the phase of the TE_{ln} and TM_{ln} modes vary as $\exp(ikz + il\theta - \omega t)$ and the azimuthal variation of the ideal helical orbits is given by $\theta \sim k_w z$, the beam resonance condition is $\omega \simeq (k + lk_w)v_z$ and both the TE_{ln} and TM_{ln} modes resonate at the lth Doppler upshift.

It should be remarked that such higher harmonic interactions do not depend upon a corresponding higher harmonic component in the single-particle orbits. In view of this, simulation runs were made for the TE_{21} mode, and growth rates were found to be comparable to those for the TE_{11} mode at approximately half the frequency. The saturation efficiency, however, was found to be greatly reduced relative to the TE_{11} mode.

In view of the high efficiencies found for the 35-GHz examples shown, important future areas of investigation include the detailed scaling of the saturation efficiency at a given frequency with such parameters as the beam energy and the wiggler parameters. The extremely high efficiencies found for parameters associated with high axial field group-II trajectories lend particular importance to a determination of the operational limits of this regime. Finally, it should also be noted that these results have been obtained for a monoenergetic electron beam, and the inclusion of a finite energy spread in the simulation is currently being pursued.

ACKNOWLEDGMENTS

This work was supported in part by the U. S. Office of Naval Research and in part by the U.S. Naval Electronic Systems Command. The authors would like to thank R. K. Parker, R. H. Jackson, and A. T. Drobot for helpful discussions.

*Permanent address: Science Applications, Inc., McLean, VA 22102.

[1]L. R. Elias, W. M. Fairbanks, J. M. J. Madey, H. A. Schwettman, and T. I. Smith, Phys. Rev. Lett. **36**, 717 (1976).

[2]D. A. G. Deacon, L. R. Elias, J. M. J. Madey, G. J. Ramian, H. A. Schwettman, and T. I. Smith, Phys. Rev. Lett. **38**, 892 (1977).

[3]V. L. Granatstein, S. P. Schlesinger, M. Herndon, R. K. Parker, and J. A. Pasour, Appl. Phys. Lett. **30**, 384 (1977).

[4]D. B. McDermott, T. C. Marshall, S. P. Schlesinger, R. K. Parker, and V. L. Granatstein, Phys. Rev. Lett. **41**, 1368 (1978).

[5]R. K. Parker, R. H. Jackson, S. H. Gold, H. P. Freund, V. L. Granatstein, P. C. Efthimion, M. Herndon, and A. K. Kinkead, Phys. Rev. Lett. **48**, 238 (1982).

[6]S. H. Gold, W. M. Black, H. P. Freund, V. L. Granatstein, R. H. Jackson, P. C. Efthimion, and A. K. Kinkead, Phys. Fluids **26**, 2683 (1983).

[7]R. W. Warren, B. E. Newman, J. G. Winston, W. E. Stein, L. M. Young, and C. A. Brau, IEEE J. Quantum Electron. **QE-19**, 391 (1983).

[8]M. Billandon, P. Elleaume, J. M. Ortega, C. Bazin, M. Bergher, M. Velghe, Y. Petroff, D. A. G. Deacon, K. E. Robinson, and J. M. J. Madey, Phys. Rev. Lett. **51**, 1652 (1983).

[9]J. Edighoffer, G. R. Neil, C. E. Hess, T. I. Smith, S. W. Fornaca, and H. A. Schwettman, Phys. Rev. Lett. **52**, 344 (1984).

[10]J. Fajans, G. Bekefi, Y. Z. Yin, and B. Lax, Phys. Rev. Lett. **53**, 246 (1984).

[11]T. J. Orzechowski, B. Anderson, W. M. Fawley, D. Prosnitz, E. T. Scharlemann, S. Yarema, D. Hopkins, A. C. Paul, A. M. Sessler, and J. Wurtele, Phys. Rev. Lett. **54**, 889 (1985).

[12]R. M. Phillips, IRE Trans. Electron Devices **7**, 231 (1960).

[13]P. Sprangle and R. A. Smith, Phys. Rev. A **21**, 293 (1980).

[14]I. B. Bernstein and J. L. Hirshfield, Phys. Rev. A **20**, 1661 (1979).

[15]R. C. Davidson and H. S. Uhm, Phys. Fluids **23**, 2076 (1980).

[16]L. Friedland and J. L. Hirshfield, Phys. Rev. Lett. **44**, 1456 (1980).

[17]I. B. Bernstein and L. Friedland, Phys. Rev. A **23**, 816 (1981).

[18]H. S. Uhm and R. C. Davidson, Phys. Fluids **24**, 1541 (1981).

[19]H. S. Uhm and R. C. Davidson, Phys. Fluids **24**, 2348 (1981).

[20]H. P. Freund, P. Sprangle, D. Dillenburg, E. H. da Jornada, R. S. Schneider, and B. Liberman, Phys. Rev. A **26**, 2004 (1982).

[21]L. Friedland and A. Fruchtman, Phys. Rev. A **25**, 2693 (1982).

[22]W. A. McMullin and R. C. Davidson, Phys. Rev. A **25**, 3130 (1982).

[23]H. P. Freund, S. Johnston, and P. Sprangle, IEEE J. Quantum Electron. **QE-19**, 322 (1983).

[24]H. P. Freund and A. K. Ganguly, Phys. Rev. A **28**, 3438 (1983).

[25]L. Friedland, Phys. Fluids **23**, 2376 (1980).

[26]P. Diament, Phys. Rev. A **23**, 2537 (1981).

[27]H. P. Freund and A. T. Drobot, Phys. Fluids **25**, 736 (1982).

[28]J. Fajans, D. Kirkpatrick, and G. Bekefi (unpublished).

[29]H. P. Freund, Phys. Rev. A **27**, 1977 (1983).